7

X-ray absorption of the mercury distribution in metal-halide lamps

Abstract. Spatial temperature profiles of metal-halide lamps have been acquired using x-ray absorption of the Hg density distribution. The temperature profiles were determined by combining the measured absorption of the spatially resolved Hg density with the wall temperature. The data analysis of x-ray absorption is extensive. After the necessary image reconstruction, the line integrated density profile needs to be Abel inverted. The solution from the Abel inversion is stabilized with the Tikhonov regularization parameter. The previous method for x-ray absorption developed in our group has been modified and improved by utilising the following 1) a larger outer bulb, 2) the corrections for x-ray scattering on the lamp materials, 3) an optimum value of Tikhonov regularisation parameter μ, 4) employing a higher degree of polynomials used for the Abel inversion. For a similar lamp as reported previously by X. Zhu [1] we found an axis temperature that is 6200 K instead of 5200. The higher temperature is similar to what is found using optical spectroscopic methods. Typical results from a metal-halide lamp with and without salts are shown.

submitted for publication in Journal of Physics D.

Figure 7.1: Colour separation in a metal-halide lamp burner. The lamp is burned vertically upright. See figure 1.1 for full colour.

7.1 Introduction

The metal-halide lamp [2] originated from the need to improve the colour properties and efficiency of the high pressure Hg lamp by adding other metals to the discharge. The metals improve spectral balance and therewith the colour properties and aid luminous efficacy. These metals are added in the form of metal-halide salts, in order to protect the burner wall and to increase the vapour pressure [3]. The metal-halide lamp contains a buffer gas of Hg and a relatively small amount of a mixture of metal-halide additives such as DyI_3, CeI_3 and/or NaI salts, which supply the prime radiators. At least two salt components are necessary for a good colour rendering index, therefore mixtures such as (NaI + ScI_3), (NaI + TlI +InI) or (NaI + TlI + DyI_3 +HoI_3 + TmI_3) are commonly used in metal-halide lamps. Due to the competition between diffusive and convective processes these additives are non-uniformly distributed over the lamp, which in a vertical burning position results in a undesirable segregation of colours [4], see figure 7.1.

For a proper understanding of the relation between the plasma transport phenomena and the energy coupling of high intensity discharge (HID) lamps we need insight in the temperature distribution over the plasma. Therefore x-ray absorption was used to measure the distribution of Hg atoms. This is done by irradiating the lamp with x-rays and by detecting the absorption of the x-ray photons in the whole lamp-burner. A temperature profile at different axial positions of the discharge can then be obtained by applying the ideal gas law combined with the wall temperature.

The application of x-ray absorption spectroscopy has the following advantages: Firstly, x-ray photons can penetrate all regions of the lamp. Secondly, the x-ray absorption cross-section depends only weakly on the electronic or chemical state of the atom. Thirdly, x-ray absorption measurements only depend on the absolute density of the detected element.

Other plasma parameters such as electron density, electron temperature, do not influence the absorption directly. [5]

Previous measurements were performed by Fohl *et al* [6] and Curry *et al* [5]. The temperature for the latter was calibrated using an optical technique to determine the axis temperature. Our approach is different in the sense that the obtained relative temperature field is calibrated with an absolute measurement of the wall temperature. The temperature that is acquired can therefore be considered a pure gas-temperature, obtained without the use of any optical techniques that is based on the interpretation of emission spectra. It is therefore of interest to compare the results with that of optical emission spectroscopy measurements [7], which yield the electron (excitation) temperature. This will give insight in a possible deviation from local thermal equilibrium [8].

The XRA experiment on metal-halide lamps asks for high spatial resolution, high dynamic range and a more or less monochromatic x-ray spectrum. Also data-analysis is complex as the absorption signal of Hg is relatively small compared to the absorption signal of the quartz wall material. Moreover, the lamp materials give rise to scattering of the x-rays, resulting in an offset. This offset is not constant over the lateral position. Finally the image itself needs to be processed and reconstructed.

The experiment and data-handling was designed by Zhu [1]. The temperature profiles she reported had an axis-to wall ratio of about 3.6. There is a discrepancy between this ratio and the ratio that was obtained from the temperature profile measured by means of optical emission spectroscopy on a nominally identical lamp [9]. These optical emission measurements showed an axis temperature that, combined with the wall temperature as measured by Zhu [1], led to a ratio of 4.6 [9].

The current study is an extension of the work of Zhu and is especially dedicated to the improvement of the data analysis. Phenomena such as beam-hardening and x-ray scattering on quartz have been studied and the latter incorporated. The inverse procedure used to extract radial information from the line-of-sight measurements was extended and implemented.

This chapter is organized as follows. Section 7.2 describes the image processing and fitting procedures necessary to obtain the temperature of the arc. Section 7.3 describes the lamps used in the experiments and the experimental setup. Results from the experiments are presented and discussed in section 7.4. These results include important improvements made to the data analysis and two temperature distributions for a lamp with and without salt filling (i.e. DyI_3). Finally, section 7.5 offers conclusions and future plans.

7.2 Theory

7.2.1 Image processing and reconstruction

The basic process of XRA is that due to the interaction with inner-shell electrons x-ray photons are removed from the beam. Since the density of the buffer gas Hg is much larger than that of the other species, the primary observable is the Hg density distribution n_{Hg}.

Therefore we can use the ideal gas law $p = n_{Hg}kT$ to translate the n_{Hg}-field into a spatial temperature profile [5]. This profile is calibrated with a wall temperature measurement. The wall temperature was measured by infra-red pyrometry using the known emissivity of the burner material [1].

The x-ray absorption measurement of the Hg concentration in metal-halide lamps requires two images: one for the lamp on and the other for the lamp off. By taking the ratio of these images, the absorption of Hg is obtained for each line-of-sight, i.e. for each lateral position. The radial density profile can then be reconstructed by using an inversion procedure called Abel inversion [5]. However, before we can take the ratio of the on-and off images, we have to correct for a variety of image-disturbing influences that are caused by each part of the three-component setup.

The setup consists of three parts: the x-ray source for lamp irradiation, the lamp itself, and the CCD camera for imaging. Each of these components gives cause for its own disturbance of the image. These are listed as follows [1].

The source

1. is of finite dimension that leads to a blurring of the image;
2. has a divergent cone-like beam that makes the CCD image larger than the object;
3. has a non-monochromatic spectrum which will cause a "beam-hardening" effect.

The lamp

1. will shift and expand due to the temperature rise in the on-situation;
2. brings an offset signal due to scattering of the x-rays.

The CCD camera

1. has a dark current;
2. has a non-uniform pixel sensitivity.

Therefore several corrections have to be made in the data-handling before subtraction of the logarithmic on- and off images can take place and Abel inversion can be applied.

We will first focus on the imperfections of the source. The point-source character of the x-ray source causes the image to be magnified. A coordinate transformation is necessary to acquire the correct lateral position needed for the Abel inversion, see [1]. However, since the x-ray source is not a perfect point source but of finite dimension this also results in blurring of the image. We tried to reduce blurring by using a deconvolution technique but we found that this was counter productive as the noise level was increased, so no deconvolution was applied. Beam-hardening [1] has been avoided by choosing an acceleration voltage that results in a quasi-monochromatic beam. Measurements were performed and reported in section 7.4 to examine the severity of this effect.

The lamp itself also causes difficulties in the image reconstruction. The lamp has an unstable position and will move and expand after it is switched on. The thermal expansion also causes the density of the burner wall to decrease. The result of this is that the on-image will have a slightly higher intensity than the off-image. This means that the difference of the absorption between lamp-on and lamp-off can not only be attributed to the presence of an Hg vapour. When the lamp is on, the burner shifts, rotates and expands, a correction is made for these effects in the fitting procedure.

7.2.2 Fitting procedure

The signal on the CCD camera that is created by the intensity of the x-ray beam that, after being partially absorbed by the lamp material reads,

$$I(x, E) = I_0(E)e^{-\tau(x,E)} \tag{7.1}$$

where E equals the photon energy, $I_0(E)$ the intensity of the source, x is the lateral position, and τ the optical depth. The optical depth τ, which is a dimensionless quantity which can be described as $\tau = kd$ with k the absorption coefficient and d the depth; it can also be written as $\tau = \rho\sigma_\rho d$ with σ_ρ the mass absorption coefficient and ρ mass the density. The optical depth has basically has three contributions that it originates from, first the outer bulb, second the wall material of the burner and third the Hg vapour. As we are mainly interested in the Hg vapour the first two contributions have to be removed. This is done by means of lamp-off measurements. The contribution of the outer bulb is minor and is removed before the burner is fitted. The outer bulb curvature is fitted with a parabola which is then subtracted to give a straight profile outside the burner. For the sake of convenience the optical depth of the wall material is cast in an analytical expression of the function

$$y = -ln(I) \tag{7.2}$$

For the lamp-off situation we can describe the fitting function for two different regions, inside the burner, $0 \leq |x - x_0| < r_1$ and inside the burner wall: $r_1 \leq |x - x_0| \leq r_2$, see figure 7.2 [1];

$$y^{off}(x) = y_0^{off} - 2k\left(\sqrt{r_2^2 - (x - x_0)^2} - \sqrt{r_1^2 - (x - x_0)^2}\right), 0 \leq |x - x_0| < r_1 \tag{7.3}$$

$$y^{off}(x) = y_0^{off} - 2k\left(\sqrt{r_2^2 - (x - x_0)^2}\right), r_1 \leq |x - x_0| \leq r_2 \tag{7.4}$$

where k is an absorption coefficient independent of position. By fitting the experimental data with a non-linear least-squares fit (Levenberg-Marquardt [10]), the parameters y_{off}, k, x_0, r_1, r_2 are found. Especially the r_1-value is important, since it defines the inner-burner wall, which is the boundary of the Abel inversion procedure later in the data-handling.

Before the τ-value of the lamp-off can be subtracted we have to transform the on-fitting function y_0 into y_0^* given by [1]

$$y^{*on}(x, \mathbf{c}) = c_4 + c_3[y^{on}(c_1 x + c_2)] \tag{7.5}$$

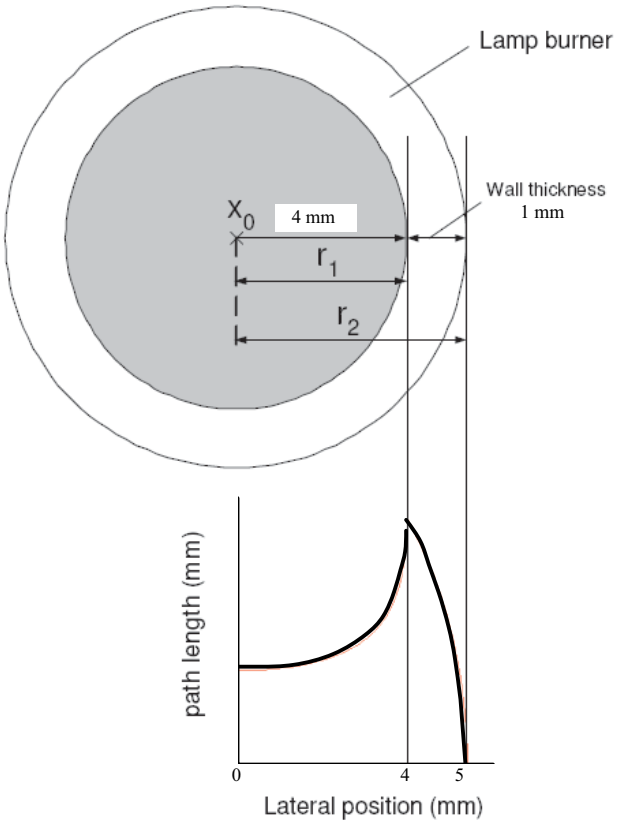

Figure 7.2: The path length through the burner as a function of lateral position [1]. The burner inner radius $r_1 = 4$mm, the burner outer radius $r_2 = 5$mm.

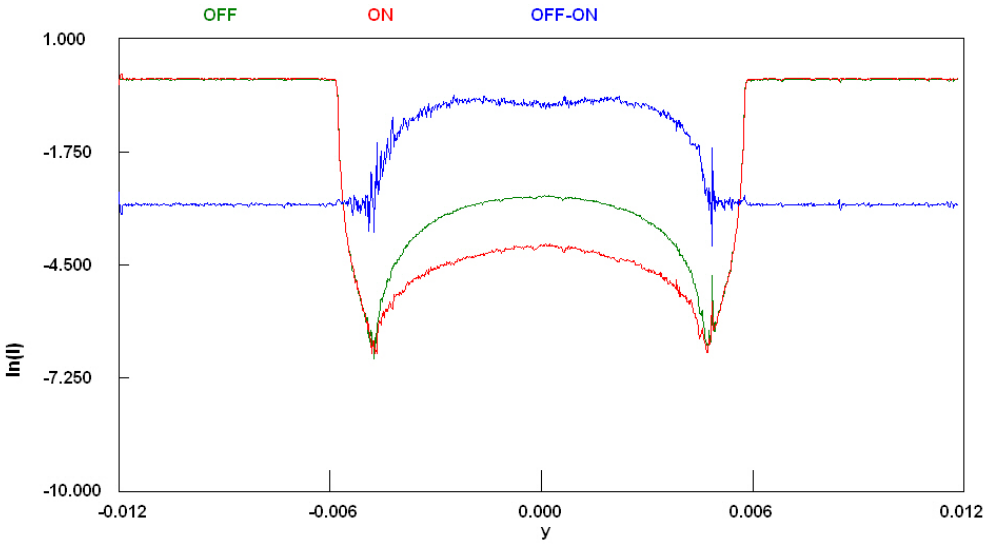

Figure 7.3: Lamp-on and off fitting of at one axial position, the difference between the fitted lamp-on and off profile, also shown, provides the absorption contribution of Hg. The line showing the difference between the on-and off profiles has been moved up by -3 and enlarged for clarity.

Where fitting-vector $\mathbf{c} = (c_1, c_2, c_3, c_4)$ corrects for the expansion and shift of the burner after the lamp is switched on. c_1 corrects for expansion, c_2 for the burner shift, c_3 for the wall-density decrease (due to expansion), c_4 for both dose-inequality (difference between x-ray dose produced by the source between on-and off measurements) and density decrease. These values for $\mathbf{c}$ are found using the same non-linear least-squares fitting method as for the off-profile fitting of equations 7.3 and 7.4.

The total fitting procedure is as follows. First the lamp-off data is fitted using equations 7.3 and 7.4 which yields y_{off}, k, x_0, r_1 and r_2. Then the lamp-on data is fitted using equation 7.4 in the area outside the burner-inner wall $|x - x_0| > r_1$, yielding r_1, r_2, x_0 for the lamp-on situation and therefore the initial values for c_1 and c_2 in equation 7.5. These values are then used to determine the density decrease and offset c_3, c_4 and c_1, c_2 by fitting the on-profile onto the off-profile in the area $r_1 < |x - x_0| < r_2$.

The scattering correction was recently introduced in order to correct for the offset I_{off} of the measured intensity profile I_{meas} caused by the scattering of the x-ray photons on the quartz. The offset is subtracted from the measured intensity

$$I = I_{meas} - I_{off}, \tag{7.6}$$

during fitting, thereby adjusting equation 7.2. The laterally integrated Hg density profile $F(x)$ can now be found using [1], see figure 7.3,

$$F(x) = \frac{y^{off}(x) - y^{*on}(x)}{c_3 \overline{\sigma}_{Hg}} \tag{7.7}$$

where $\overline{\sigma}_{Hg}$ is the mean absorption cross-section of Hg [1].

7.2.3 Tikhonov regularized Abel inversion

Radial information can be extracted from the lateral profile $F(x)$ with the Abel inversion procedure. The radial density function is represented by the even-order polynomial function

$$n(r) = \sum_{i=0}^{N} a_{2i} r^{2i} \tag{7.8}$$

The column density $F(x)$ can be described as [11]

$$F(x) = 2 \cdot \sum_{i=0}^{N} a_{2i} h_{2i}(x) \tag{7.9}$$

where N determines the order of the fitting-function, i.e. the number of h_{2i}-terms

$$h_{2i}(x) = \int_{x}^{R} \frac{r^{2i+1}}{\sqrt{r^2 - x^2}} dr \tag{7.10}$$

The coefficients a_{2i} are evaluated from the data $f_{meas}(x_k)$, which is measured at M points, using a least square estimation

$$\sum_{k=1}^{M} (F(x_k) - f_{meas}(x_k))^2 \rightarrow min \tag{7.11}$$

The partial derivative of this condition to the unknown coefficients a_{2i} yields a set of equations. [11]

$$\sum_{i=1}^{N} a_{2(i-1)} \sum_{k=1}^{M} h_{2(m-1)}(x_k) h_{2(i-1)}(x_k) = \sum_{k=1}^{M} h_{2(m-1)}(x_k) f_{meas}(x_k) \tag{7.12}$$

In matrix notation this can be written as

$$\mathbf{M} \cdot \mathbf{a} = \mathbf{b} \tag{7.13}$$

where $\mathbf{a}$ is given by $(a_0, ..., a_N)^T$ and where $\mathbf{b}$ is the measured data f_{meas} and can be written as

$$\mathbf{b} = (b_1, .., b_N)^T, \ where \ b_m = \sum_{k=1}^{M} h_{2(m-1)}(x_k) f_{meas}(x_k) \tag{7.14}$$

and $\mathbf{M}$ contains the even-order fitting-polynomials and is given by

$$M_{mi} = \sum_{k=1}^{M} h_{2(m-1)}(x_k) h_{2(i-1)}(x_k), \ for \ 1 \leq m \leq N, 1 \leq i \leq N \tag{7.15}$$

where $\mathbf{M}$ is

$$\begin{pmatrix} M_{11} & M_{12} & ... & M_{1N} \\ M_{21} & M_{22} & ... & M_{2N} \\ ... & ... & ... & ... \\ M_{N1} & M_{N2} & ... & M_{NN} \end{pmatrix}$$

Equation 7.13 can also be written as

$$\mathbf{M}^T\mathbf{M} \cdot \mathbf{a} = \mathbf{M}^T \cdot \mathbf{b} \tag{7.16}$$

Now the unknown coeffients a_{2i} can be found by

$$\mathbf{a} = (\mathbf{M}^T\mathbf{M})^{-1}\mathbf{M}^T \cdot \mathbf{b} \tag{7.17}$$

It would seem that large N (order of fitting function) would be sufficient to fit the data, however, because of the high noise level in the data near the wall, the fit tends to oscillate around the noise instead of following the actual profile. This can be remedied by using a regularisation method that allows for the dampening of such oscillations. A trade-off then needs to be made between the 'size' of the regularised solution and the quality of the fit that it provides to the given data [12]. The regularisation method used to stabilise the solution is called Tikhonov regularisation [13]. Now the fitting parameters $\mathbf{a}$ can be found by

$$\mathbf{a} = (\mathbf{M}^T\mathbf{M} + \mu I)^{-1}\mathbf{M}^T \cdot \mathbf{b} \tag{7.18}$$

where $\mathbf{M}^T$ denotes the transposed matrix (which is equal to $\mathbf{M}$ due to symmetry), μ the Tikhonov parameter which restricts all solutions to the ones with minimum norm. In the inverse procedure, two types of errors are introduced, the approximation error and the noise-propagation error. Since the approximation error increases with μ, whereas the noise-propagation error decreases with μ, there is an optimum value of μ for the inverse problem. A numerical test has to be made for each case in order to get an optimum μ value.

7.3 Experimental setup

A quasi-monochromatic x-ray beam generated by the Mo-anode x-ray tube (equipped with a Zr filter), is directed towards the metal-halide lamp under investigation, see figure 7.4. Part of the radiation will be absorbed while the remaining photons are detected by an x-ray CCD camera. CCD images are taken for two situations, a burning lamp (lamp on) and a non-burning lamp (lamp off). In the off-situation, the Hg is not present in the volume of the burner, but is condensed in small droplets on the wall or (usually) on the electrodes. When the lamp is burning, it is filled with Hg vapour. The Hg in the lamp-on situation causes an additional absorption of the x-ray photons. Therefore, the difference of the absorption signal between the lamp-on and lamp-off cases gives information about the Hg density. In the following sections we discuss the setup, consisting of a source and CCD camera, and the lamp used for the experiments.

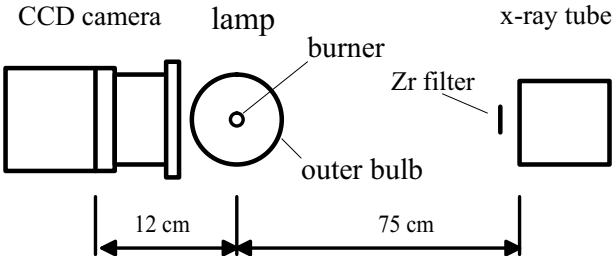

Figure 7.4: Top view of the x-ray absorption spectroscopy setup. The setup consists of a CCD camera, an x-ray tube and a lamp. The camera is shown in more detail in figure 7.5. The entire setup is encased in a box made of lead.

7.3.1 X-ray source

A commercial x-ray source, a Philips PW 1130, initially designed for crystallography, was used for our x-ray absorption experiment of metal-halide lamps. This source has a high brightness and a small focal spot size. The system has a standard tube tower housing, in which different x-ray tubes can be installed. In our XRA experiment, the Mo-anode x-ray tube has been used. The x-ray generator/source operated at 20 mA and 25 kV with an x-ray spot size of 0.4 by 8 mm.

In order to obtain a high spatial resolution, the dimensions of the x-ray emitting area (the anode) must be as small as possible, especially in the horizontal direction, that is in the direction parallel to the lateral dimension x of the metal-halide lamp under investigation. Therefore a fine focus (FF) x-ray tube was used with a focus size of 0.4 mm by 8 mm. The 8 mm refers to the depth, this dimension pointing more or less in the direction of the x-ray source lamp. The 0.4 mm size is parallel to the lateral direction x. See [1] for more details.

To reach a good spatial resolution (100 μm) with an x-ray focal spot of relatively large dimensions (0.4 mm in lateral direction), the vertically positioned metal-halide lamp has been placed far from the source, namely at a distance of 75 cm. Typical integration time is 120 s per image, multiple images (typical 100) are taken to increase the signal to noise ratio.

The Mo anode x-ray tube has a spectrum that contains two typical Mo K-lines (Kα: 17.5 keV, Kβ: 19.6 keV). The Zr filter has a K-absorption edge at 18 keV, causing the X-ray spectrum above 18 keV to be strongly absorbed. Thus the spectrum from the X-ray source is expected to consist mainly of the Mo Kα(17.5 keV) line super-imposed on a continuous background of Bremsstrahlung radiation. The energy below 15 keV will be further attenuated by the outer bulb of the metal-halide lamp. Therefore we can assume that the spectrum of the radiation offered to the burner is quasi-monochromatic and mainly consisting of the Mo Kα line [1]. Beam-hardening occurs when the source is not monochromatic enough, this was studied by placing several slides of quartz in front of the CCD in consecutive order, the results of this test is presented in section IV.

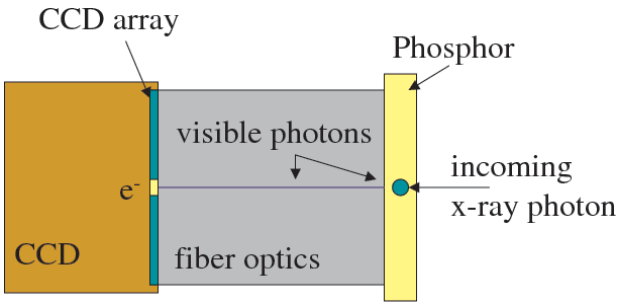

Figure 7.5: The PI-SCX1300 CCD consists of three parts, a phosphor sheet, fiber optics and the CCD array. The CCD array contains 1340 x 1300 pixels of 20μm by 20μm each.

7.3.2 CCD camera

In order to detect the x-ray photons that have passed through the metal-halide lamp we use an x-ray CCD camera, a PI SCX 1300. The crucial part of this device is a CCD-array of a type that is well-known for applications of image registration. However, since the CCD-array is not sensitive for hard x-ray radiation the x-ray quanta have to be converted into visible photons. During that conversion, effectuated by a phosphor plate, the x-ray photon generates a large number of visible photons as the energy of an x-ray photon (typically 17 keV) is much larger than that of a visible photon. [1]. Figure 7.5 shows the main parts of which of the x-ray CCD camera consists, a phosphor sheet, fiber optics and the CCD-array.

7.3.3 The lamp

The lamp consists of an 8 mm inner diameter quartz arc tube surrounded by a quartz outer bulb. The inner diameter of the outer bulb is 120 mm. This is much larger than in the previous measurements done by Zhu [1], there the outer bulb of the metal-halide COST lamp [14] [15] had an inner diameter of 20 mm. The wall thickness of both burner and outer-bulb is typically 1 mm. The benefits of a larger outer bulb are twofold. First, by using a larger outer bulb the effect of the curvature of the outer bulb on the detected absorption signal can be much better approximated with a parabolic fit. Second, there is less wall material to traverse through near the edge which results in a higher signal. The electrode gap is 18 mm. Two different lamps were investigated, one containing only 10 mg of Hg, the other 10 mg of Hg with 4 mg of DyI_3. For the measurements presented here, the lamp was operated vertically at a power of 145 W. The power was supplied by a square-wave ballast programmed at a frequency of 122 Hz.

7.4 Results and Discussion

The experiment and principle method were developed by Zhu [1] in order to obtain the temperature distribution from the measured absorption of the x-rays by the Hg in the

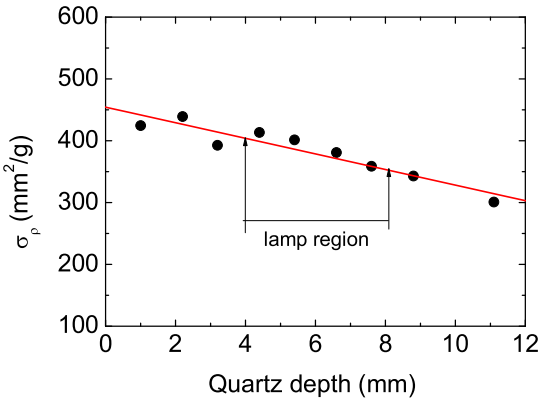

Figure 7.6: Mass absorption coefficient as a function of quartz thickness. At the centre of the burner the quartz thickness is 4mm at the wall this is 8 mm. It is shown that, due to beam-hardening, the absorption coefficient decreases for increasing path lengths; however this effect is limited as long as we stay below a quartz depth of 8 mm.

arc. However, a number of remaining problems had yet to be addressed. These are beam-hardening, scatter of x-rays by the lamp materials and an optimum value for the Tikhonov parameter μ. In this section we discuss these three aspects and the resulting temperature distribution of two lamps, without and with salt (DyI_3).

7.4.1 Beam-hardening

Beam-hardening occurs when low energy photons are absorbed more readily than high energy photons as the path length increases. As a consequence each absorbing material will act as a filter; the 'soft' (low energy) photons are removed from the beam; the 'hard' (high energy) photons remain. This not only alters the transmitted spectrum but changes the mean cross-section. For longer path-lengths the material will become relatively more transparent. This might affect the measurement near the wall of the burner, where the amount of quartz that is traversed by the x-ray is highest. To examine the significance of this effect in our measurements, a set of 10 quartz slides were placed consecutively in front of the CCD. An image was taken after each placement of a slide. The photon energy of the beam is partly absorbed by the quartz, the transmitted intensity is measured by the CCD camera and can be described as

$$I(d) = I_0(E)e^{-\sigma_\rho \cdot \rho \ d} \tag{7.19}$$

where I is the intensity of the beam, I_0 is the intensity of the beam before traversing through quartz, E the beam energy, σ_ρ the mass absorption coefficient for quartz [1], ρ the quartz mass density d and the quartz depth.

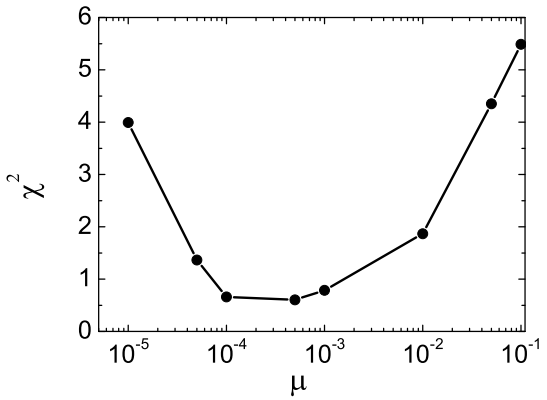

Figure 7.7: A typical curve of the chi-square as a function of the different μ-values. The minimum of the curve is found at $\mu \approx 10^{-4}$.

The mass absorption coefficient σ_ρ is plotted as a function of the quartz thickness in figure 7.6. It shows that the absorption coefficient decreases as the thickness increases. In the case of the lamp, the minimum quartz thickness that is penetrated by the x-rays is 4 mm (through the centre), the maximum is 8 mm (directly at the inner-burner wall). Figure 7.6 shows that this leads to an error of around 5% at the minimum thickness and 16% at the maximum thickness, this is comparable to the error made during fitting near the wall and can therefore be neglected. The systematic error caused by the beam-hardening effect leads to an underestimation of the axis temperature of about 10%.

7.4.2 Tikhonov regularisation parameter μ

The Abel inversion was regularised as was discussed in section 7.2.3 with Tikhonov parameter μ. The optimum value of μ was found by comparing the temperature profile generated by a model with a measured temperature profile. This model was created by R. Cornelis *et al* [16] to simulate the x-ray measurement procedure. A theoretical temperature profile, based on the one proposed by Fischer [9] was used as input data. The program then simulated the lamp images on-and off. The simulated images were then analysed using the same method as was used for the measurements. The measured temperature profile was determined with different values for μ. A chi-square evaluation was then performed for the difference between the model and experimental profiles

$$\chi^2 = \frac{1}{T_{eff} N} \sum_i \left(T^{sim} - T_i^{meas} \right)^2 , \tag{7.20}$$

where T_{eff} is the effective temperature [9] taken as 3000 K , N is the number of datapoints, and T^{sim} and T_i^{meas} are the simulated and measured temperature profile respectively.

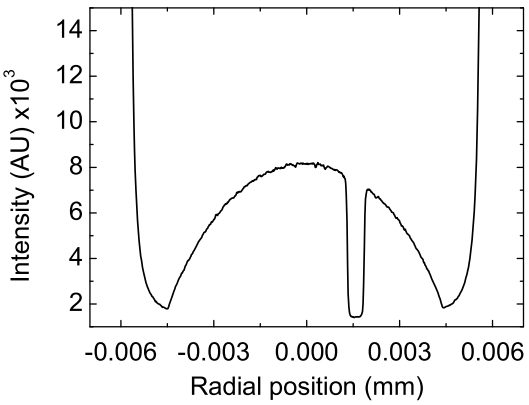

Figure 7.8: The lamp intensity after it is blocked by the messing strip, taken at the midplane of the lamp. The lamp was moved with respect to the strip.

A typical curve of the chi-square as a function of the different μ-values is shown in figure 7.7. The minimum of the curve is found at $\mu \approx 10^{-4}$. This value was subsequently used as the Tikhonov parameter for the Abel fitting of the intensity curves necessary for the calculation of the temperature profiles. Finally, 16 Abel terms were used instead of the previous 11 terms [1], allowing for a better approximation of the lateral profile.

7.4.3 Scattering of x-rays

The offset, as was discovered by X Zhu, was investigated. She found this offset when horizontal brass strips were placed in front of the camera. The strips were expected to block the signal completely, however a signal of about 14% of the unblocked signal was found [1]. This phenomenon is most likely caused by the scatter of x-ray photons by the quartz burner. This was further examined by placing a strip of 500 microns wide vertically between the CCD and the lamp. See figure 7.8. The (non-burning) lamp was then moved laterally so that the strip blocked the incoming x-rays for different horizontal positions of the lamp. The average value of the signal found behind the blocking strip as a function of lateral position is depicted in figure 7.9. The values found were used for the scattering correction in the data-analysis program. This allowed for a much better fit of the intensity profile near the wall. This part of the profile has a very steep gradient, so that an appropriate determination of this region is of the utmost importance. The new scattering correction resulted in an increase of the axis temperature with more than 1000K compared to previously reported temperature profiles [1].

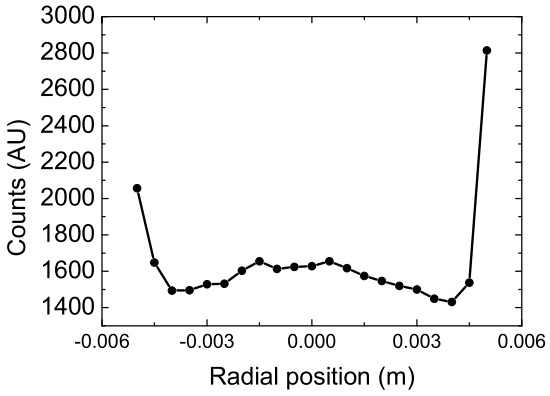

Figure 7.9: Offset found after a thin messing strip of 500 μm wide has been placed in front of the CCD camera (see figure 7.8). The lamp was moved with respect to the strip. The values found near the wall (about 1450 counts) were used for the scattering correction factor in the data analysis. This provided a much better fitting near the wall of the burner.

7.4.4 Temperature distribution

Two typical examples of a temperature distribution are shown in figure 7.10 and 7.11. Figure 7.10 shows the temperature distribution of an metal-halide lamp containing 10 mg of Hg. The axis temperature at the midplane of the lamp is 6000 K. The error is approximately 10%. Near the electrodes the arc contracts due to the shape of the electric field. In between the shape of the profile is near-parabolic.

Figure 7.11 shows the temperature distribution of an metal-halide lamp containing 10 mg of Hg and DyI_3. The axis temperature at the midplane is about 6200 K. This is more than 1000 K higher than reported by Zhu [1], but comparable to the results obtained by optical emission spectroscopy [7] [9] [18]. The ratio of the axis temperature and the wall temperature is 4.7. This is much closer to the ratio of 4.6, which was obtained with the temperature profile obtained by emission spectroscopy [9] combined with the wall temperature measurement [1], than the ratio of 3.6 measured by Zhu [1].

Like the lamp containing pure Hg, the arc contracts near the electrodes and is near-parabolic in between. However, comparing the profile close to the lower electrode to that close to the top electrode, it is clear that the profile close to the lower electrode shows more contraction [9]. Axial segregation causes most of the Dy, which is an excellent radiator, to be present at the bottom of the lamp. Dy causes the arc to cool locally near the flank of the discharge resulting in contraction [9] [18]. This contraction near the lower electrode of a nominally identical lamp was also reported by X. Zhu [1].

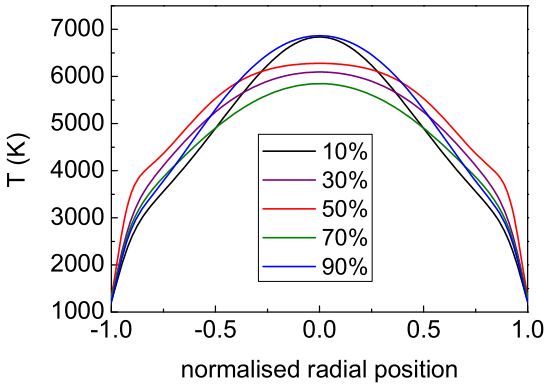

Figure 7.10: Radial temperature profiles at different axial positions for a Hg pure lamp. The radius is 4 mm and the electrode distance 18 mm. The axial positions are given as a fraction of the total arc-length starting with the bottom electrode. From top to bottom, at the central radial position, the axial positions are as follows, 90 %, 10 %, 50 %, 30 %, 70 %

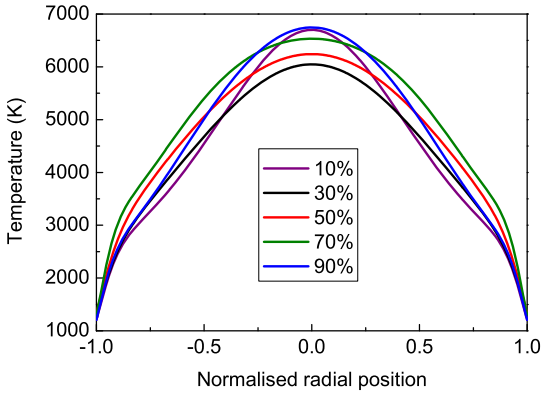

Figure 7.11: Radial temperature profiles at different axial positions for a lamp containing Hg and DyI_3. The radius is 4 mm and the electrode distance 18 mm. The axial positions are given as a fraction of the total arc-length starting with the bottom electrode. From top to bottom, at the central radial position, the axial positions are as follows, 90 %, 10 %, 70 %, 50 %, 30 %

7.5 Conclusions

The data-analysis of the x-ray absorption technique has been improved, leading to an axis temperature of about 6200 K in a metal-halide lamp containing Hg and DyI_3. This is in agreement with optical emission spectroscopy measurements done previously. The axis-to-wall temperature ratio of the x-ray absorption is also much more comparable to the emission spectroscopy measurements than earlier reported results obtained with the same setup [13]. It is the scattering of the x-rays on the quartz burners that were found to have such a profound effect. Taking this effect into account allowed for a much better fitting, causing the temperature profiles to be 1000 K higher than the previously reported temperatures of the same setup.

The Abel inversion was regularized with an optimised Tikhonov parameter $\mu = 10^{-4}$. Beam-hardening was found to be negligible, which led to the conclusion that the source is near mono-chromatic due to the combined effect of the Zr filter and the absorption of the wall material. The temperature profile of the lamp containing DyI_3 was mostly contracted near the bottom of the lamp. This is where most of the atomic Dy is present and causes local cooling of the flank of the discharge. Future plans include x-ray absorption of metal-halide lamps with a variety of fillings such as NaI, TlI, DyI_3 and a combination of these.

7.6 Acknowledgments

This research is sponsored by the Technologiestichting STW (project No. ETF 6093) and COST (project 529).

Bibliography

[1] Zhu X, PhD thesis: *active spectroscopy on HID lamps*, Eindhoven University of Technology,(2005)

[2] Lister G G, Lawler J E, Lapatovich W P and Godyak V A 2004 Rev. Mod. Phys. **76**, 541

[3] Coaton J R, Marsden A M, Lamps and Lighting, Arnold, London, 4th edition, 1997

[4] Fischer E 1976 J. Appl. Phys. **47**, 2954

[5] Curry J J, Sakai M and Lawler J E 1998 J. Appl. Phys. **84**, 3066

[6] Fohl T, Kramer J M and Lester J E 1993 J Appl Phys 73 46

[7] Nimalasuriya T, Pupat N B M, Flikweert A J, Stoffels W W, Haverlag M and Van der Mullen J J A M 2006 J. Appl. Phys. **99** 053302 **see chapter 2**

[8] J.A.M. Van der Mullen, Phys. Rep. **191** 109 (1990)

[9] Nimalasuriya T, Flikweert A J, Haverlag M, Kemps P C M, Kroesen G M W, Stoffels W W, Van der Mullen J J A M 2006 *J. Phys D: Appl Phys* **39** 2993 **see chapter 3**

[10] Press W H, Flannery B P, Teukolsky S A 1989 *Numerical recipes in Pascal, the art of scientific computing* Cambridge University Press.

[11] Pretzler G, *A New Method for Numerical Abel-Inversion*, Z. Naturforsch. 46a, 1991, pages 639-641

[12] Hansen P C, The L-curve and its use in the numerical treatment of inverse problems

[13] M.Bertero and Boccacci P 1998 Introduction to inverse problems in imaging (Bristol and Philadelphia: Institute of Physics Publishing)

[14] Stoffels W W, Flikweert A J, Nimalasuriya T, Van der Mullen J J A M, Kroesen G M W, Haverlag M, 2006 Pure Appl. Chem. **78** No 6

[15] Nimalasuriya T, Curry J J, Sansonetti C J, Ridderhof E J, Shastri S D, Flikweert A J, Stoffels W W, Haverlag M, Van der Mullen, J J A M 2007 J.Phys.D **40**, 2831 **see chapter 6**

[16] Cornelis R 2006, MSc Thesis, X-Ray Absorption measurements and measurement simulations on HID lamps, Eindhoven University of Technology

[17] Denisova N, Haverlag M, Ridderhof E J, Nimalasuriya T, Van der Mullen J J A M, to be submitted

[18] Nimalasuriya T, Thubé G M, Flikweert A J, Haverlag M, Kroesen G M W, Stoffels W W, Van der Mullen 2007, J.Phys.D 2007 **40** 2839 **see chapter 4**